The Journal of Chemical Physics

High-performance NiOOH/FeOOH electrode for OER catalysis

Cite as: J. Chem. Phys. **154**, 024706 (2021); https://doi.org/10.1063/5.0036019
Submitted: 02 November 2020 . Accepted: 23 December 2020 . Published Online: 12 January 2021

Patrick Gono, and Alfredo Pasquarello

The Journal of Chemical Physics ARTICLE scitation.org/journal/jcp

High-performance NiOOH/FeOOH electrode for OER catalysis

Cite as: J. Chem. Phys. 154, 024706 (2021); doi: 10.1063/5.0036019
Submitted: 2 November 2020 • Accepted: 23 December 2020 •
Published Online: 12 January 2021

Patrick Gono[a] and Alfredo Pasquarello

AFFILIATIONS

Chair of Atomic Scale Simulation (CSEA), Ecole Polytechnique Fédérale de Lausanne (EPFL), CH-1015 Lausanne, Switzerland

[a]Author to whom correspondence should be addressed: patrick.gono@epfl.ch

ABSTRACT

The outstanding performance of NiOOH/FeOOH-based oxygen evolution reaction (OER) catalysts is rationalized in terms of a bifunctional mechanism involving two distinct active sites. In this mechanism, the OOH_{ads} reaction intermediate, which unfavorably affects the overall OER activity due to the linear scaling relationship, is replaced by O_2 adsorbed at the active site on FeOOH and H_{ads} adsorbed at the NiOOH substrate. Here, we use the computational hydrogen electrode method to assess promising models of both the FeOOH catalyst and the NiOOH hydrogen acceptor. These two materials are interfaced in various ways to evaluate their performance as bifunctional OER catalysts. In some cases, overpotentials as low as 0.16 V are found, supporting the bifunctional mechanism as a means to overcome the limitations imposed by linear scaling relationships.

I. INTRODUCTION

In order to achieve the widespread use of hydrogen fuel in the future, efficient electrochemical water splitting is critical.[1] The water splitting process can be understood in terms of the hydrogen evolution reaction (HER) taking place on the cathode and the oxygen evolution reaction (OER) taking place on the anode. While the former is efficiently catalyzed by noble metals, such as Pt,[2] the latter is often found to limit the overall efficiency of the water splitting reaction.[3] Consequently, a great effort has gone into investigating the OER. The OER is commonly modeled as a four proton-coupled electron transfer (PCET) reaction, exhibiting the three reaction intermediates, OH_{ads}, O_{ads}, and OOH_{ads},[4,5]

$$\begin{aligned} 1: &\quad H_2O_{(\ell)} \longrightarrow OH_{ads} + H^+ + e^-, \\ 2: &\quad OH_{ads} \longrightarrow O_{ads} + H^+ + e^-, \\ 3: &\quad O_{ads} + H_2O_{(\ell)} \longrightarrow OOH_{ads} + H^+ + e^-, \\ 4: &\quad OOH_{ads} \longrightarrow O_{2\,ads} + H^+ + e^-. \end{aligned} \tag{1}$$

From a thermodynamic perspective, the ideal anode material forms bonds with the above intermediates so that the Gibbs free energies ΔG_i, $i \in \{1, 2, 3, 4\}$ of the four PCET steps equal to 1.23 eV.[6] However, both the computational work and experimental work point to the existence of linear scaling relationships between the binding energies of the reaction intermediates that ultimately limit the efficiency of the OER.[7] The most pertinent linear scaling relationship can be understood in terms of the similar character of the OH_{ads} and the OOH_{ads} intermediate and can be quantified by the relation $\Delta G_2 + \Delta G_3 = 3.2$ eV.[5]

Therefore, in order to overcome the limitations set by this scaling relationship, alternative reaction mechanisms have been considered in which the problematic OOH_{ads} intermediate is eliminated. One such approach is a bifunctional OER mechanism involving two functionally distinct active sites.[8–12] Notably, this bifunctional reaction mechanism has been proposed as an explanation for the low OER overpotentials observed on nickel/iron oxyhydroxide electrodes.[13] In this mechanism, the unfavorable OOH_{ads} intermediate rapidly splits apart, thus forming the O_2 species at one active site and a H_{ads} intermediate adsorbed at another active site,

$$\begin{aligned} 1: &\quad H_2O_{(\ell)} \longrightarrow OH_a + H^+ + e^-, \\ 2: &\quad OH_a \longrightarrow O_a + H^+ + e^-, \\ 3: &\quad O_a + H_2O_{(\ell)} \longrightarrow H_b + O_2 + H^+ + e^-, \\ 4: &\quad H_b \longrightarrow H^+ + e^-, \end{aligned} \tag{2}$$

where *a* refers to the first active site accommodating most of the reaction intermediates and *b* refers to the hydrogen accepting second active site. Nickel oxyhydroxide has attracted considerable attention on account of the high OER activities when doped with iron.[14–16] To understand the low OER overpotentials of these FeNiOOH catalysts, the detailed role of iron impurities in NiOOH has been addressed.[17,18] It is assumed that iron atoms are substituted for nickel, forming $Fe_xNi_{1-x}OOH$ compounds, with the value of x ranging between 0.1 and 0.25.[17,19,20] The identification of the active site stimulates an ongoing discussion with several studies pointing to iron as the active site for the catalysis.[15,21,22] In contrast, a recent computational study identified an undercoordinated edge nickel atom to exhibit the lowest overpotential.[12] However, the iron and nickel compounds that are of interest here can also combine in different ways. Song *et al.* rationalized the high OER activity rates of their electrode in terms of the synergy between catalytically active γ-FeOOH nanoparticles and a γ-NiOOH substrate acting as a hydrogen acceptor.[11]

In this work, we present a systematic study of NiOOH, FeOOH, and their interfaces and evaluate their potential as possible catalysts within the bifunctional scheme given in Eq. (2) using the computational hydrogen electrode (CHE) method. First, the two materials are studied separately, and suitable models are constructed for both of them. Next, all combinations of the studied models are investigated in order to determine the most suitable pairings for the catalysis of the OER according to the bifunctional mechanism. Finally, the best performing pairings are used to build interfaces between FeOOH and NiOOH, which are then studied regarding their performance within the bifunctional reaction scheme.

II. METHODOLOGY

The CHE method is adopted in order to calculate the free energy steps corresponding to the PCET reactions. The free energy difference ΔG corresponding to the reaction $A \rightarrow B + H^+ + e^-$ is given by

$$\Delta G \equiv \mu[B] - \mu[A] + \tfrac{1}{2}\mu\left[H_{2\,(g)}\right], \tag{3}$$

where the chemical potential of the proton–electron pair is replaced by one half of the chemical potential of hydrogen gas. The chemical potential of a species A is calculated as

$$\mu[A] = E_{\mathrm{DFT}} + \mathrm{ZPE} - TS + \Delta U^{0\rightarrow T}, \tag{4}$$

where E_{DFT} is the total energy of the system achieved using density functional theory (DFT), ZPE is the zero point energy of the vibrational degrees of freedom of the nuclei, S is the entropy, and $\Delta U^{0\rightarrow T}$ is the internal energy at temperature T. In the case of free species, the entropy and internal energy consist of vibrational, rotational, and translational contributions. In the case of adsorbed species, all degrees of freedom are assumed to be vibrational, and therefore, only the vibrational contributions are retained. The vibrational modes are calculated by performing a geometry optimization and a subsequent finite difference vibrational analysis. In the case of adsorbed species, we evaluate the vibrational modes only for one of the FeOOH interface models, as the relaxed structures of the adsorbates obtained for the various surfaces studied here differ only marginally. The entropy (TS) and internal energy ($\Delta U^{0\rightarrow T}$) terms are calculated at a temperature of 293.15 K. A more detailed description of the thermodynamic corrections can be found in Chapter 10 of Ref. 23.

The values of the thermodynamic corrections, ZPE, TS, and $\Delta U^{0\rightarrow T}$, obtained for each species considered here are given in Table I. Once the free energy steps ΔG for each of the four reaction steps in Eqs. (1) or (2) are obtained, the reaction overpotential η is calculated as $\eta \equiv \max_i\{\Delta G_i - 1.23\}$ for $i \in \{1, 2, 3, 4\}$.

All DFT calculations are carried out using the CP2K suite of codes.[24,25] The Perdew–Burke–Ernzerhof (PBE) approximation to the exchange and correlation functional is adopted.[26] The rVV10 functional is used to account for van der Waals interactions.[27] Triple-zeta quality MOLOPT basis sets[28] and analytical Goedecker–Teter–Hutter pseudopotentials[29] are used for all elements. The plane wave representation of the electron density uses a cutoff of 700 Ry. In all cases, the lowest possible total spin projection is considered for the unrestricted Kohn–Sham calculations. This choice was found to minimize the total energy in the case of a benchmark lepidocrocite FeOOH layer system.

During the geometry optimization, all atoms are allowed to move. Within this approach, the free energy of the overall OER is found to be $\Delta G_{\mathrm{OER}} = 4.22$ eV. This value underestimates the experimental value of $\Delta G^{\mathrm{exp}}_{\mathrm{OER}} = 4.92$ eV. It is commonly assumed that this is due to a limitation of the semilocal density functional in describing the O_2 molecule.[30] Hence, a correction of 0.70 eV is added to the total energy of the $O_{2(g)}$ species. In this way, the overall reaction free energy is consistent with the experimental value of ΔG_{OER}.

The OER is taking place at the anode, where valence band holes are present. Following Ref. 31, we model effective anodic conditions by subtracting the bandgap of the substrate from the total energy of the H_{ads} intermediate when evaluating the binding energy of hydrogen. This procedure is rationalized in terms of the electron donated by H_{ads} to the substrate upon adsorption. In neutral conditions, the additional electron populates the closest available unoccupied level, which is found above the bandgap in the case of a semiconducting

TABLE I. The thermodynamic corrections for all adsorbed and free species considered in this work. From left to right: zero point energy ZPE, entropy contribution TS, internal energy change $\Delta U^{0\rightarrow T}$, and the total correction given by $E_{\mathrm{corr}} \equiv \mathrm{ZPE} - TS + \Delta U^{0\rightarrow T}$. All values are in eV.

System	ZPE	TS	$\Delta U^{0\rightarrow T}$	E_{corr}
OH_{ads}	0.37	0.06	0.04	0.35
O_{ads}	0.08	0.04	0.03	0.06
OOH_{ads}	0.47	0.14	0.08	0.41
H_{ads}	0.30	0.01	0.01	0.29
$H_{2(g)}$	0.19	0.42	0.09	−0.13
$H_2O_{(\ell)}$	0.55	0.65	0.10	−0.00
$O_{2(g)}$	0.07	0.59	0.09	−0.42

slab. At variance, in anodic conditions, i.e., in the presence of valence band holes, the electron occupies a state near the valence band maximum. The binding energy of the OH_{ads}, O_{ads}, and OOH_{ads} intermediates has been found to be unaffected by the adoption of anodic conditions, and hence, no further modification is required in these cases.

III. RESULTS AND DISCUSSION

This section is organized as follows. First, the FeOOH and NiOOH catalysts are addressed separately, and appropriate computational models are constructed. FeOOH is studied as a potential OER catalyst, whereas NiOOH is evaluated as a potential hydrogen acceptor in the bifunctional OER scheme.

A. Computational models for FeOOH and NiOOH

In regard to FeOOH, two polymorphs are investigated. Both exhibit a layered structure of edge-sharing FeO_6 octahedra. The first is γ-FeOOH, or lepidocrocite, and exhibits an orthorhombic crystal structure.[32] The second studied polymorph is the one adopted in the computational models of Song *et al.*,[11] in which the octahedra are arranged in layers consistent with a trigonal symmetry. Both supercells are relaxed in order to obtain the optimized lattice parameters and the corresponding total energies. We find that lepidocrocite is more stable than the other polymorph by 0.04 eV per atom, neglecting entropic effects. Hence, only the lepidocrocite structure is considered in all further calculations.

To assess the performance of γ-FeOOH in the context of the OER, we use the CHE method to calculate the free energy steps corresponding to the regular mechanism, which proceeds through the OH_{ads}, O_{ads}, and OOH_{ads} intermediates. Several possible γ-FeOOH configurations are studied. All the systems studied present exposed surface iron atoms and are thus suitable to act as catalysts. The experimental evidence points toward small FeOOH nanoparticles as the main catalytically active systems.[11,13] Hence, many different facets are expected to be present in a realistic model. Moreover, the relative stability of the various possible surface terminations needs to be addressed under realistic conditions, i.e., in the presence of solvent and under potential bias. Besides, given the finite size of the simulated systems, different surface terminations may strongly affect the overall stoichiometry of the model system and, in this way, introduce errors in the evaluation of the relative surface phase stability.

In light of the resulting complications, both technical and conceptual, we here investigate how the overpotential η could vary for a selection of FeOOH models. First, a slab model is built by exposing the (100) facet of the bulk supercell to 20 Å of vacuum. This model is adopted on account of the exposed Fe atoms along edges of the FeOOH layers. The (001) facet has been found to lead to high OER overpotentials in previous studies and is thus not considered here.[33] Three possible surface terminations are considered: a surface with all Fe atoms being bare, an O covered surface, and an OH covered surface. In the latter two cases, the active site for the OER catalysis is created by exposing a single surface iron atom through the removal of a surface O atom or OH group, respectively. The studied structures are shown in Figs. 1(a)–1(c). Second, a layer model is obtained by isolating a single lepidocrocite layer from the slab model with adjacent layers being separated by 20 Å of vacuum due to the periodicity of the simulation cell. Again, three edge terminations are investigated. In the first, the edge consists of exposed Fe atoms. In the second and third, the edge is terminated by O atoms and OH groups, respectively. In the case of the bare-edged layer, we find that the topology of the structure is not preserved upon relaxation. The sizable structural reorganizations prevent the meaningful evaluation of the binding energies of the reaction intermediates, which are central to the CHE method. Therefore, the layered model with a bare edge is disregarded. Third, a nanocluster model is considered. Due to the large configuration space, we limit ourselves to clusters consisting of four FeO_6 octahedra extracted from the lepidocrocite structure. Figure 1(d) shows one of the considered γ-FeOOH nanoclusters. Three cluster models are investigated in total: the first with all surface oxygen atoms covered with hydrogen [$Fe_4O(OH)_{15}$], the second with a single hydrogen atom removed [$Fe_4O_2(OH)_{14}$], and the third with two hydrogen atoms removed [$Fe_4O_3(OH)_{13}$].

All structures corresponding to the slab, the layer, and the nanocluster models are relaxed. A surface iron atom is exposed by design unless already bare and is considered as the active site in the regular OER mechanism. The binding energies of the OH_{ads}, O_{ads}, and OOH_{ads} intermediates are evaluated, and the OER free energy steps are calculated. Given the similar configurations of the adsorbates, we assume the thermodynamic corrections in Table I to be identical

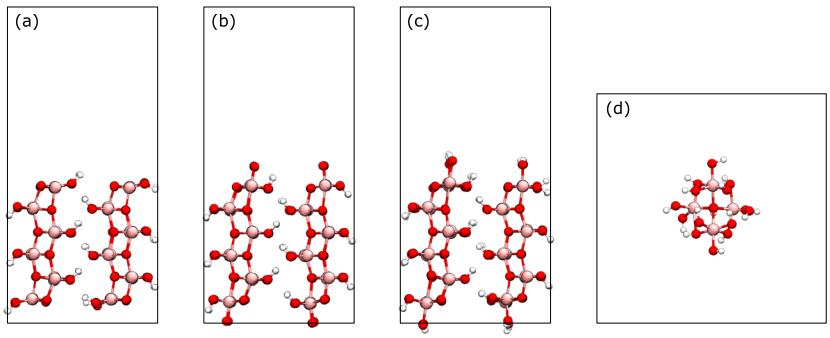

FIG. 1. The FeOOH structures considered in this work. (a) Bare γ-FeOOH with Fe atoms exposed on the (100) facet, (b) O covered slab, and (c) OH covered slab. The layer configurations are obtained by isolating a single layer from each respective slab structure. (d) FeOOH nanocluster. The iron atoms are shown in pink, the oxygen atoms are shown in red, and the hydrogen atoms are shown in white.

in all studied models. The final free energy steps for each studied model are given in Table II. Some of the present structures turn out to be favorable candidates within the bifunctional OER scheme on account of the first and second free energy steps being approximately equal to 1.23 eV, with the third reaction step being the limiting one.[31] In particular, the O terminated lepidocrocite layer and the fully hydrogen covered nanocluster [$Fe_4O(OH)_{15}$] show promise.

We study NiOOH as a potential hydrogen acceptor in order to evaluate the free energy steps following the bifunctional OER mechanism. Two polymorphs are generally studied in connection with the OER: β-NiOOH and γ-NiOOH.[16,22,34–37] Both exhibit a trigonal symmetry and consist of NiO_2 layers. In β-NiOOH, the interlayer spacing is small, and one half of the oxygen atoms in the NiO_2 layers are hydrogenated, forming OH groups. In the case of γ-NiOOH, the distance between the layers is large enough for water molecules to intercalate the NiO_2 sheets. Apart from water molecules, electrolyte ions are presumed to be present as well, with concentrations of up to 33%.[36,38] The γ-NiOOH phase is often considered as the active phase during the OER.[17,39] However, in this work, NiOOH is assumed to only act as a substrate and as an H acceptor. Given that both the β and γ phase consist of the same layers, and in light of the complexity and the absence of a detailed characterization of the γ-NiOOH structure, we focus solely on β-NiOOH. It is believed that Ni ions with an average oxidation number of at least 3.5 are present at OER conditions.[36,40] Therefore, in computational models of γ-NiOOH, one third of the intercalated neutral water molecules is often replaced by positively charged ions, such as Na^+, in order to achieve the desired Ni oxidation state.[16,36,41] In contrast, the effective Ni charge state in the adopted β-NiOOH model can be tuned by changing the stoichiometry of the slab through the addition or removal of hydrogen atoms. In this sense, the simpler β-NiOOH model adopted here captures the main features of the more complex γ-NiOOH phase.

Orthorhombic slab models consisting of one, two, three, four, and five layers are built exposing the (001) facet of NiOOH. For each choice of slab thickness, we consider two possible surface terminations: (*i*) a bare outermost NiO_2 layer and (*ii*) a partially hydrogen covered surface layer. In the latter case, the overall stoichiometry of NiOOH is preserved. The NiOOH systems will from now on be designated with an integer specifying the number of layers.

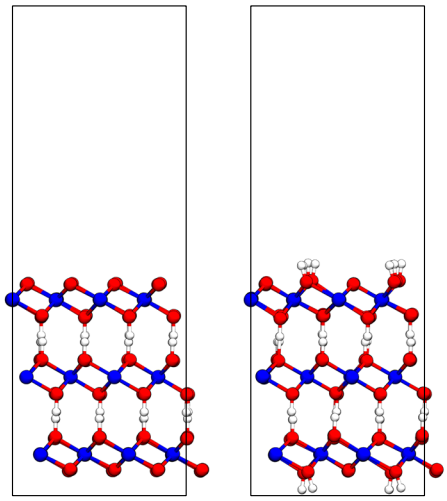

FIG. 2. Three-layer thick slab model of NiOOH with a bare surface (3NiOOH, left) and a partially hydrogen covered surface [3NiOOH(s), right] such that the overall NiOOH stoichiometry of the system is preserved.

Configurations with a partially hydrogen covered surface exhibiting the stoichiometry of bulk NiOOH are further designated with (s). Figure 2(a) illustrates the two surface terminations studied here in the case of the three-layer thick NiOOH slab.

In all cases, an exposed surface oxygen atom is assumed to be the hydrogen acceptor. All structures are relaxed, and the hydrogen binding energy is calculated. Anodic conditions are modeled by subtracting the calculated bandgap from the total energy of the hydrogen adsorbate H_{ads}.[31] The hydrogen adsorption free energies are given in Table III.

The stoichiometric NiOOH configurations are found to bind hydrogen more weakly than the configurations with bare surfaces, and the corresponding binding energies show an increasing trend with the number of layers. In contrast, the calculated binding energies calculated at the slabs with bare surfaces decrease with increasing slab thickness, and the observed trend is much larger in magnitude. This can be understood in terms of the average oxidation state of Ni, which decreases with every additional slab layer for the

TABLE II. The free energy steps ΔG_i corresponding to the regular OER mechanism in Eq. (1) for all studied FeOOH systems. All values are in eV.

System	ΔG_1	ΔG_2	ΔG_3	ΔG_4
Slab	0.76	0.90	1.92	1.30
O covered slab (slab O)	0.00	1.92	0.81	2.16
OH covered slab (slab OH)	0.78	1.61	1.22	1.27
O terminated layer (layer O)	0.97	1.09	1.86	0.96
OH terminated layer (layer OH)	0.00	1.47	1.48	1.94
$Fe_4O(OH)_{15}$	1.27	0.98	2.52	0.11
$Fe_4O_2(OH)_{14}$	1.39	1.67	1.40	0.41
$Fe_4O_3(OH)_{13}$	0.95	2.04	1.53	0.35

TABLE III. The hydrogen adsorption free energy $\Delta G[H_{ads}]$ for each NiOOH configuration. To model anodic conditions, the bandgap of the dehydrogenated system is subtracted from the total energy of the hydrogenated system in the calculation of the adsorption free energy.[31] All values are in eV.

Number of layers	Bare surface	Stoichiometric
1	−1.94	−0.81
2	−1.49	−1.00
3	−1.41	−1.04
4	−1.32	−1.09
5	−1.28	−1.10

non-stoichiometric bare surface models. For the larger slabs, the difference between the models with the bare and the partially hydrogen covered surface is smaller due to the fact that the bare surface model approaches the bulk NiOOH stoichiometry with every additional layer. The last step of Eq. (2) represents the removal of the hydrogen atom. Hence, the associated free energy difference ΔG_4 is the opposite of the hydrogen adsorption free energy $\Delta G_4 = -\Delta G[H_{ads}]$. The closer $\Delta G[H_{ads}]$ is to the water splitting potential of 1.23 eV, the more promising the material as a hydrogen acceptor within the bifunctional scheme. Ultimately, out of the studied systems, the five-layer NiOOH system with the bare surface is the most favorable, indicating that thicker layers are generally more suitable for this reaction mechanism.

B. Bifunctional NiOOH/FeOOH catalyst

First, the catalytic performance of the NiOOH/FeOOH catalysts in the bifunctional scheme is studied by considering the FeOOH system associated with site *a* and the NiOOH system associated with site *b* in separate computational cells. The hydrogen adsorption free energy in Table III represents the negative of ΔG_4 in the bifunctional mechanism. The first two steps, ΔG_1 and ΔG_2, of both the regular mechanism and the bifunctional mechanism in Eq. (2) are identical. Finally, given that the overall OER free energy is $\Delta G_{OER} = 4.92$ eV, the third step ΔG_3 can be calculated as $\Delta G_3 = 4.92 - \Delta G_1 - \Delta G_2 - \Delta G_4$. Hence, combining the results for FeOOH listed in Table II and for NiOOH in Table III, we obtain the free energy steps corresponding to the bifunctional mechanism for all combinations of the studied systems. The reaction overpotential η for each pairing of FeOOH and NiOOH is shown in Fig. 3(a). Figure 3(b) draws a comparison between the overpotential achieved with the regular mechanism and the overpotential in the bifunctional scheme. Some combinations of a FeOOH system and a NiOOH substrate exhibit overpotentials above the volcano imposed by the linear scaling relationships. In particular, the combination of the fully hydrogen covered FeOOH nanocluster [$Fe_4O(OH)_{15}$] and the four-layer thick bare slab of NiOOH exhibits an overpotential of only 0.11 V. The best performing pairings of the bifunctional catalysts are shown in a two-dimensional volcano plot in Fig. 3(c). Here, the calculated overpotential is shown as a function of the oxygen $\Delta G[O_{ads}]$ and the hydrogen $\Delta G[H_{ads}]$ binding energies. Assuming the linear scaling relationships $\Delta G_2 + \Delta G_3 = 3.2$ eV and $\Delta G[O_{ads}] = 2\Delta G[OH_{ads}]$, the theoretically achievable overpotential within the bifunctional scheme can be parametrized using only $\Delta G[O_{ads}]$ and $\Delta G[H_{ads}]$ and is given as background in Fig. 3(c). The most favorable pairings identified here can be found near the top of the bifunctional volcano, and the corresponding overpotentials calculated here are generally in good agreement with the theoretical overpotential plotted in the background.

The study of the three cluster models, which only differ in the number of hydrogen atoms, shows how sensitive these systems are to the oxidation states of the iron atoms. The presence of hydrogen atoms has a twofold effect. First, the extra electron of each additional hydrogen atom affects the oxidation state of the active iron site. Second, the hydrogen atoms participate in the formation of hydrogen bonds with nearby oxygen atoms, including the OER intermediates. It appears that decreasing the number of hydrogen atoms (and thereby increasing the oxidation state of the active site) leads to the increase of the second ΔG_2 and to the reduction of the third ΔG_3 free energy step, shifting the position of the cluster from the left side of the volcano to the right side in Fig. 3(b). While $Fe_4O_2(OH)_{14}$ exhibits the lowest overpotential in the regular OER mechanism, it

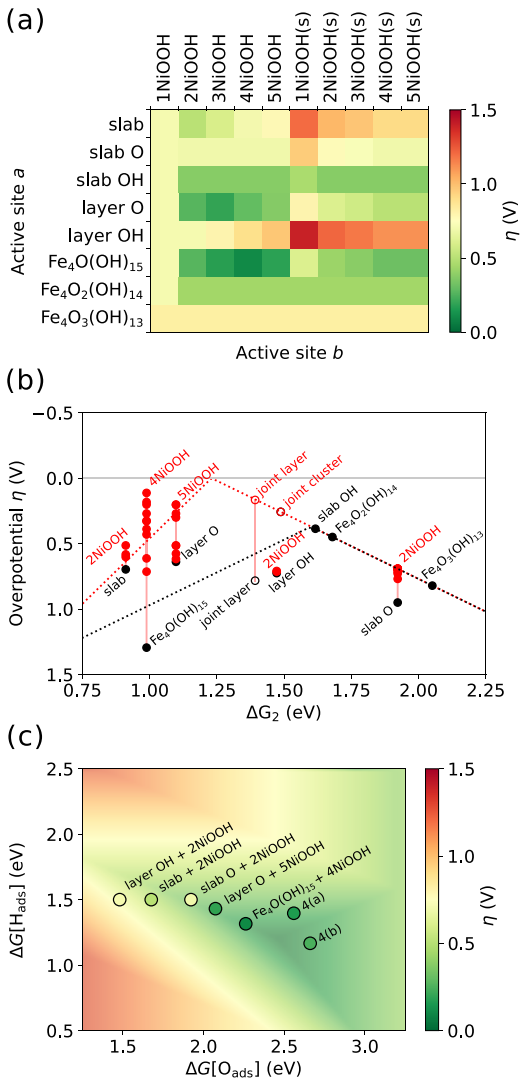

FIG. 3. (a) The OER overpotential η for each combination of a FeOOH configuration acting as active site *a* and a NiOOH system acting as site *b* within the bifunctional OER scheme. The green color signifies a pairing of systems with a very low overpotential. (b) Volcano plot of the OER overpotential η as a function of ΔG_2. The black dots correspond to the regular mechanism, and the labels refer to the respective FeOOH system. The red dots correspond to the bifunctional mechanism, and the labels are only shown for the NiOOH system that leads to the lowest η. The open black (red) symbols correspond to η achieved for the joint FeOOH/NiOOH systems following the regular (bifunctional) mechanism. The dotted lines represent the linear scaling relationships $\Delta G_2 + \Delta G_3 = 3.2$ eV and $\Delta G[O_{ads}] = 2\Delta G[OH_{ads}]$.[5,7] (c) A two-dimensional volcano plot of η following the bifunctional mechanism. Only the best performing pairings of catalysts are shown. The background colors represent the theoretical overpotential achieved from the linear scaling relationships.

is $Fe_4O(OH)_{15}$, the nanocluster with all surface O atoms covered by hydrogen, which proves to be the most favorable in the bifunctional scheme.

Given the impressive performance of some pairings of FeOOH and NiOOH when considered separately, the next question that arises is how these catalysts perform when explicitly interfaced. The five-layer thick NiOOH slab with bare surfaces shows a near optimal hydrogen binding energy of 1.28 eV (see Table III) and is hence considered as the substrate. The lepidocrocite layer with oxygen terminated edges and the fully hydrogen covered nanocluster [$Fe_4O(OH)_{15}$] are taken as the potential FeOOH nanoparticle models. In the first case, we build a joint model consisting of the five-layer thick NiOOH slab and of the O-terminated FeOOH layer physisorbed on its surface. The interface with the NiOOH substrate can be formed in a straightforward manner on account of the match between the lattice parameter of lepidocrocite and the dimensions of the orthorhombic NiOOH supercell. However, covalent bonds between the layer and the NiOOH substrate are not possible due to incompatible crystal structures. The optimized configuration of the physisorbed layer model is shown in Fig. 4(a). In the second case, a covalent bond between the NiOOH substrate and the FeOOH nanocluster is considered, as suggested in the work of Song *et al.*[11] The cluster is adsorbed through a single bond between an iron atom in the cluster and a NiOOH surface oxygen atom. The optimized structure is shown in Fig. 4(b). Following the suggestion by Song *et al.*, we consider the iron atom bound to the surface as the active site.[11] The OER free energy steps are calculated from the binding energies of all reaction intermediates and are given in Table IV. The reaction overpotentials corresponding to both the regular and bifunctional mechanisms are shown in Figs. 3(b) and 3(c).

In the case of the physisorbed FeOOH layer [Fig. 4(a)], the free energy steps corresponding to both reaction mechanisms are similar to those achieved for the FeOOH layer and NiOOH substrate taken separately. The OER overpotential η in the bifunctional scheme is found to be as low as $\eta = 0.16$ V. First, this result suggests that the proximity of the two van der Waals bound catalysts may lead to only a minor modification of the free energy steps achieved with separate computational cells for each material [see Fig. 3(b)]. Second, the overpotential of 0.16 V is well above the volcano in Fig. 3(b), which lends further support to the bifunctional mechanism as a means of overcoming the limitations imposed by the linear scaling relationship. Despite exhibiting a slightly higher overpotential, the covalently bound γ-FeOOH nanocluster [Fig. 4(b)] is of interest in relation to the work of Song *et al.*[11] There, an iron atom attached to the NiOOH substrate was identified experimentally as the active site of a novel bifunctional catalyst for the OER. The γ-FeOOH nanocluster covalently bound to a NiOOH substrate studied here may therefore reproduce the main structural features of the unconventional catalyst observed in the aforementioned work. In particular, the active site is indeed an iron atom covalently bound to the (001) facet of the NiOOH substrate. This iron site is part of an FeO_6 octahedron, which is tilted at an angle of 50° with respect to the NiO_6 octahedra of the substrate, in good agreement with the experimental value of 52° reported in Ref. 11. Moreover, while the distance between the active iron atom and the closest Ni atoms of the substrate is around 3.5 Å, the next nearest neighbors can be found at a distance of about 4.5 Å. This is in line with the EXAFS spectra corresponding to a dry sample under neutral conditions reported in Ref. 11. The present system also leads to an overpotential of just 0.25 V in both the regular and bifunctional mechanisms. While this value is larger than in the case of FeOOH and NiOOH treated in separate computational cells [0.15 V, see Figs. 3(a) and 3(b)], it nevertheless is in good agreement with the experimental overpotentials reported in Ref. 11. Studies of similar systems have achieved overpotentials following the regular OER mechanism comparable to the value of $\eta = 0.25$ V obtained here.[42] However, this does not rule out the bifunctional reaction scheme in Eq. (2) as the OER mechanism at the NiOOH/FeOOH electrode.

Song *et al.* suggested that the FeOOH nanoparticles in their experiments are 1 nm–2 nm in size, at least twice as large as the nanoclusters studied here. The small size of the studied clusters may lead to an unphysically large reorganization of the atoms upon adsorption of the reaction intermediates. This, in turn, may affect the binding energies and the observed trends in the free energies. In order to estimate this effect on the calculated free energies in the case of the covalently bound FeOOH nanocluster, we re-evaluate the geometry optimizations with all metal atoms kept fixed, with the sole exception of the iron atom acting as the active site. In this way, the size, the orientation, and the structure of the nanocluster remain largely unchanged during the OER. Hence, this procedure allows us to model the conditions of a larger cluster, which would undergo a more limited reorganization. This system is referred to as

TABLE IV. The free energy steps ΔG_i following the regular and the bifunctional OER mechanism, as well as the OER overpotential η, for both studied NiOOH/FeOOH interfaces. All free energy values are in eV.

System	ΔG_1	ΔG_2	ΔG_3	ΔG_4	η (V)
Joint layer regular	1.16	1.39	2.01	0.33	0.78
Joint layer bifunctional	1.16	1.39	0.95	1.39	0.16
Joint cluster regular	1.17	1.48	0.97	1.27	0.25
Joint cluster bifunctional	1.17	1.48	1.07	1.16	0.25
Joint cluster fixed regular	1.07	1.50	1.27	1.04	0.27
Joint cluster fixed bifunctional	1.07	1.50	1.17	1.14	0.27

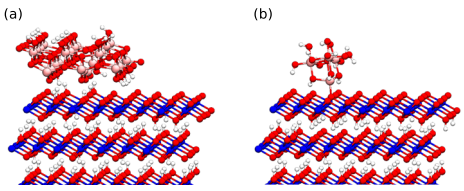

FIG. 4. Interfaces between the five-layer thick NiOOH slab and the studied FeOOH configurations: (a) lepidocrocite layer with oxygen terminated edges physisorbed on NiOOH (referred to as the *joint layer*) and (b) covalently bound FeOOH nanocluster (referred to as the *joint cluster*). The iron atoms are shown in pink, the oxygen atoms are shown in red, the nickel atoms are shown in blue, and the hydrogen atoms are shown in white.

joint cluster fixed, and the resulting OER free energy steps are given in the last two rows of Table IV. The free energy steps following the regular OER mechanism are affected by at most 0.3 eV, while the bifunctional OER steps obtained for the fixed model are within 0.1 eV of the results obtained for the fully relaxed one. However, for both mechanisms, the second free energy step ΔG_2 is the reaction limiting one, and the calculated overpotential is nearly identical between the fixed (0.27 V) and fully relaxed (0.25 V) models. Hence, the effect of the reorganization related to the small size of the cluster is found to be negligible.

Finally, we discuss the effect of the solvent. A recent computational study on a related Fe doped NiOOH catalyst highlights the critical importance of explicitly modeling the water solvent when considering the bifunctional mechanism.[12] The observed effect is twofold. First, the water facilitates the transport of hydrogen, enabling the third reaction step of the bifunctional mechanism,[12] i.e., the inclusion of the solvent facilitates the transfer of the H atom from the OOH_{ads} intermediate to the second active site on the hydrogen acceptor, where H_{ads} is formed. Second, the presence of water molecules can stabilize or destabilize the OER intermediates and, in this way, affect the calculated free energy steps. This aspect deserves attention as it questions the CHE method used in this work. The inclusion of explicit water in static calculations has been observed to greatly modify the calculated binding energies of OER intermediates. However, this effect is usually overestimated on account of the frozen nature of the water and the absence of entropic effects.[43] In a study focusing on TiO_2, the effect of liquid water on the OER free energy steps was found to be more modest.[44] Moreover, the observed effect was rationalized in terms of an electrostatic stabilization of the charge distributions localized at a dielectric interface. In the case of the regular mechanism, a sizable effect was only observed for ΔG_2 and ΔG_3 due to the doubly charged nature of the O_{ads} intermediate present in both reaction steps. Meanwhile, reaction steps that involve solely singly charged intermediates were found to be only weakly affected by the presence of the solvent. Focusing on the bifunctional mechanism, we assume that the effect of the solvent is mainly dictated by the same electrostatic considerations. In particular, the Wannier center analysis of the calculated wave functions corresponding to the NiOOH system with the covalently bound FeOOH nanocluster shows that only O_{ads} is doubly charged (attracting two electrons from the bulk), whereas both OH_{ads} and H_{ads} are singly charged, localizing a single electron and hole, respectively. This is in line with the findings obtained for the intermediates of the regular mechanism, indicating that both the regular and bifunctional mechanisms can be treated in the same fashion. Finally, in order to assess how relevant the results obtained in the case of TiO_2 are for the NiOOH/FeOOH systems studied here, a model dielectric system is built representing the five-layer thick NiOOH slab. We determine the dielectric constant of the slab to be $\epsilon \approx 30$ through the use of a finite electric field.[45] This value is slightly higher than that of rutile TiO_2 ($\epsilon \approx 24$).[44] Hence, in the case of NiOOH, the electrostatic effect of the solvent on the OER free energies is expected to be similar, or even smaller, than in the case of TiO_2. As a consequence, ΔG_1 and ΔG_4 should remain unchanged upon the inclusion of the solvent. The steps involving the doubly charged intermediate O_{ads}, namely, ΔG_2 and ΔG_3, should be affected to a similar degree, as observed in the case of TiO_2.[44] Moreover, ΔG_2 and ΔG_3 in both the regular and bifunctional mechanisms are expected to be equally affected by the presence of water. Hence, the relative performance of the two mechanisms as described by our results should be reliable even in the absence of the solvent.

IV. CONCLUSION

In conclusion, we have studied a selection of NiOOH and FeOOH systems in order to assess their performance in the bifunctional catalysis of the OER. We have identified several promising models both for the FeOOH catalyst and for the NiOOH substrate acting as the hydrogen acceptor. Explicit interfaces between these materials have been constructed. Calculations carried out within the CHE scheme showed overpotentials as low as 0.16 V for some of these interfaces. Our thermodynamical study supports the bifunctional mechanism as a possible explanation of the low overpotentials observed for NiOOH/FeOOH catalysts during the OER.

ACKNOWLEDGMENTS

We thank C. Corminboeuf and M. Busch for useful interactions and a critical reading of the manuscript. This work has been realized in relation to the National Center of Competence in Research (NCCR) "Materials' Revolution: Computational Design and Discovery of Novel Materials (MARVEL)" of the SNSF. We used computational resources of the Swiss National Supercomputing Centre (CSCS grant under Project Nos. s879 and mr24) and of the Scientific IT and Application Support Center (SCITAS) of the Ecole Polytechnique Fédérale de Lausanne.

DATA AVAILABILITY

The data that support the findings of this study are openly available in the Materials Cloud repository https://doi.org/10.24435/materialscloud:ex-va

REFERENCES

[1] R. D. Tentu and S. Basu, Curr. Opin. Electrochem. **5**, 56 (2017).
[2] N. Cheng, S. Stambula, D. Wang, M. N. Banis, J. Liu, A. Riese, B. Xiao, R. Li, T.-K. Sham, L.-M. Liu, G. A. Botton, and X. Sun, Nat. Commun. **7**, 13638 (2016).
[3] Z. W. Seh, J. Kibsgaard, C. F. Dickens, I. Chorkendorff, J. K. Nørskov, and T. F. Jaramillo, Science **355**, eaad4998 (2017).
[4] Á. Valdés, Z.-W. Qu, G.-J. Kroes, J. Rossmeisl, and J. K. Nørskov, J. Phys. Chem. **112**, 9872 (2008).
[5] I. C. Man, H. Y. Su, F. Calle-Vallejo, H. A. Hansen, J. I. Martínez, N. G. Inoglu, J. Kitchin, T. F. Jaramillo, J. K. Nørskov, and J. Rossmeisl, ChemCatChem **3**, 1159 (2011).
[6] K. Maeda and K. Domen, Chem. Lett. **1**, 2655 (2010).
[7] M. T. M. Koper, J. Electroanal. Chem. **660**, 254 (2011).
[8] N. B. Halck, V. Petrykin, P. Krtil, and J. Rossmeisl, Phys. Chem. Chem. Phys. **16**, 13682 (2014).
[9] M. Busch, N. B. Halck, U. I. Kramm, S. Siahrostami, P. Krtil, and J. Rossmeisl, Nano Energy **29**, 126 (2016).
[10] M. Busch, Curr. Opin. Electrochem. **9**, 278 (2018).
[11] F. Song, M. M. Busch, B. Lassalle-Kaiser, C.-S. Hsu, E. Petkucheva, M. Bensimon, H. M. Chen, C. Corminboeuf, and X. Hu, ACS Cent. Sci. **5**, 558 (2019).

[12]M. Vandichel, K. Laasonen, and I. Kondov, Top. Catal. **63**, 833 (2020).
[13]L. Bai, S. Lee, and X. Hu, "Spectroscopic and electrokinetic evidence for a bifunctional mechanism of the oxygen evolution reaction," Chemie (published online, 2020).
[14]T. Safdari, N. Akbari, A. Valizadeh, R. Bagheri, Z. Song, S. I. Allakhverdiev, and M. M. Najafpour, New J. Chem. **44**, 1517 (2020).
[15]D. Friebel, M. W. Louie, M. Bajdich, K. E. Sanwald, Y. Cai, A. M. Wise, M.-J. Cheng, D. Sokaras, T.-C. Weng, R. Alonso-Mori, R. C. Davis, J. R. Bargar, J. K. Nørskov, A. Nilsson, and A. T. Bell, J. Am. Chem. Soc. **137**, 1305 (2015).
[16]H. Xiao, H. Shin, and W. A. Goddard, Proc. Natl. Acad. Sci. U. S. A. **115**, 5872 (2018).
[17]L. Trotochaud, S. L. Young, J. K. Ranney, and S. W. Boettcher, J. Am. Chem. Soc. **136**, 6744 (2014).
[18]S. Lee, L. Bai, and X. Hu, Angew. Chem. **132**, 8149 (2020).
[19]V. Fidelsky and M. C. Toroker, Phys. Chem. Chem. Phys. **19**, 7491 (2017).
[20]L. Trotochaud, J. K. Ranney, K. N. Williams, and S. W. Boettcher, J. Am. Chem. Soc. **134**, 17253 (2012).
[21]B. Hunter, J. Winkler, and H. Gray, Molecules **23**, 903 (2018).
[22]J. M. P. Martirez and E. A. Carter, J. Am. Chem. Soc. **141**, 693 (2019).
[23]C. J. Cramer, *Essentials of Computational Chemistry: Theories and Models*, 2nd ed. (Wiley, Chichester, 2004), pp. 355–366.
[24]J. VandeVondele, M. Krack, F. Mohamed, M. Parrinello, T. Chassaing, and J. Hutter, Comput. Phys. Commun. **167**, 103 (2005).
[25]J. Hutter, M. Iannuzzi, F. Schiffmann, and J. VandeVondele, Science **4**, 15 (2014).
[26]J. P. Perdew, K. Burke, and M. Ernzerhof, Phys. Rev. Lett. **77**, 3865 (1996).
[27]O. A. Vydrov and T. Van Voorhis, J. Chem. Phys. **133**, 244103 (2010).
[28]J. VandeVondele and J. Hutter, Chem. Phys. **127**, 114105 (2007).
[29]S. Goedecker, M. Teter, and J. Hutter, Phys. Rev. B **54**, 1703 (1996).
[30]J. K. Nørskov, J. Rossmeisl, A. Logadottir, L. Lindqvist, J. R. Kitchin, T. Bligaard, and H. Jónsson, J. Phys. Chem. **108**, 17886 (2004).
[31]P. Gono and A. Pasquarello, J. Chem. Phys. **152**, 104712 (2020).
[32]Z. Huang, F. Han, M. Li, Z. Zhou, X. Guan, and L. Guo, Comput. Mater. Sci. **169**, 109110 (2019).
[33]M. Tang and Q. Ge, Chin. J. Catal. **38**, 1621 (2017).
[34]J. Zaffran and M. C. Toroker, ChemElectroChem **4**, 2764 (2018).
[35]A. J. Tkalych, K. Yu, and E. A. Carter, J. Phys. Chem. C **119**, 24315 (2015).
[36]Y.-F. Li and A. Selloni, ACS Catal. **4**, 1148 (2014).
[37]A. Govind Rajan, J. M. P. Martirez, and E. A. Carter, J. Am. Chem. Soc. **142**, 3600 (2020).
[38]R. Oesten, M. Wohlfahrt-Mehrens, S. Ströbele, M. Kasper, and R. A. Huggins, Ionics **2**, 293 (1996).
[39]M. Gong and H. Dai, Nano Res. **8**, 23 (2015).
[40]J. C. Conesa, J. Phys. Chem. C **120**, 18999 (2016).
[41]J. Zaffran, M. B. Stevens, C. D. M. Trang, M. Nagli, M. Shehadeh, S. W. Boettcher, and M. Caspary Toroker, Chem. Mater. **29**, 4761 (2017).
[42]Y. Zhou and N. López, ACS Catal. **10**, 6254 (2020).
[43]J. A. Gauthier, C. F. Dickens, L. D. Chen, A. D. Doyle, and J. K. Nørskov, J. Phys. Chem. **121**, 11455 (2017).
[44]P. Gono, F. Ambrosio, and A. Pasquarello, J. Phys. Chem. C **123**, 18467 (2019).
[45]P. Umari and A. Pasquarello, Phys. Rev. Lett. **89**, 157602 (2002).